Neutrophils actively swell to potentiate rapid migration

Tamas L Nagy[1,2,§], **Evelyn Strickland**[1,2], **Orion D. Weiner**[1,2]

***For correspondence:** iam@tamasnagy.com (TLN); orion.weiner@ucsf.edu (ODW)

Present address: [§]Department of Neurology, University of California Los Angeles, Los Angeles, CA, USA

[1]Department of Biochemistry and Biophysics, University of California San Francisco, San Francisco, CA, USA; [2]Cardiovascular Research Institute, University of California San Francisco, San Francisco, CA, USA

Abstract While the involvement of actin polymerization in cell migration is well-established, much less is known about the role of transmembrane water flow in cell motility. Here, we investigate the role of water influx in a prototypical migrating cell, the neutrophil, which undergoes rapid, directed movement to sites of injury and infection. Chemoattractant exposure both increases cell volume and potentiates migration, but the causal link between these processes is not known. We combine single cell volume measurements and a genome-wide CRISPR screen to identify the regulators of chemoattractant-induced neutrophil swelling, including NHE1, AE2, PI3K-gamma, and CA2. Through NHE1 inhibition in primary human neutrophils, we show that cell swelling is both necessary and sufficient for the potentiation of migration following chemoattractant stimulation. Our data demonstrate that chemoattractant-driven cell swelling complements cytoskeletal rearrangements to enhance migration speed.

Introduction

Cells extend their membranes during morphogenesis and movement. Membrane extension in plant and fungal cells is thought to require coordination between water influx and cell wall remodeling (***Boyer and Silk*** (***2004***); ***Lew*** (***2011***)). In animal cells that lack cell walls, most research has focused on the role of cytoskeletal rearrangements during membrane extension and migration (***Svitkina*** (***2018***)), though in some contexts water influx also appears to suffice for cell movement (***Stroka et al.*** (***2014***); ***Zhang et al.*** (***2022***)). It is likely that cytoskeletal rearrangements and water influx collaborate in a wider range of cell morphological and migratory contexts than are currently appreciated.

In contrast to the extensive work characterizing the actin regulators that underlie cell motility, we have a relatively poor understanding of the molecular regulators of water influx during cell migration. We address this question in neutrophils, which are innate immune cells that polarize their actin assembly and actomyosin contractility to move to sites of injury and infection (***Weiner et al.*** (***1999***); ***Sengupta et al.*** (***2006***); ***Lämmermann et al.*** (***2013***)). Chemoattractant stimulation also initiates water influx and cell swelling (***Grinstein et al.*** (***1986***)), but the molecular basis of this swelling and its relevance to motility are not known.

Results

Chemoattractant stimulation elicits competing volume responses in primary human neutrophils

Neutrophils are a powerful system to study the biophysical demands of cell motility, as they acutely initiate rapid migration following stimulation with chemoattractant. Normally, they exist in a quiescent non-motile state (***Metzemaekers et al.*** (***2020***)). Upon exposure to chemoattractants, neutrophils respond with significant morphological changes (***Sengupta et al.*** (***2006***); ***Denk et al.*** (***2017***)), water influx (***Grinstein et al.*** (***1986***); ***Pember et al.*** (***1983***)), and a dramatic increase in motility (***Martin et al.*** (***2015***)).

To probe the role of transmembrane water flow in chemoattractant-stimulated morphogenesis and movement, we adapted Fluorescence eXclusion Microscopy (FxM) (***Cadart et al.*** (***2017***)), a single cell volume measurement technique, to primary human neutrophils (***Figure 1***A; ***Figure 1—figure Supplement 1***A-E). This assay enables us to accurately measure absolute cell volume in single primary human neutrophils during activation by chemoattractant (***Figure 1***B-C). We used a UV-sensitive caged chemoattractant (***Collins et al.*** (***2015***)) to acutely stimulate the cells in situ with a short (10s) pulse of light enabling us to capture both the volume and motility response of cells before and after activation. Following chemoattractant-uncaging, the cells spread and transformed into a motile, amoeboid state with high persistence (***Figure 1***C). By simultaneously measuring the single cell volumes, we observed a biphasic volume response (***Figure 1***D; ***Video 1***). Immediately following chemoattractant exposure, the cells lose 5-8% of their cell volume (***Figure 1***D, inset), consistent with spreading-induced volume losses previously observed in several other cell types (***Venkova et al.*** (***2022***)). Following this spreading-mediated initial volume loss, the cells swelled significantly, reaching a median volume 15% larger than their resting volumes after 20 minutes, agreeing with previous reports (***Grinstein et al.*** (***1986***); ***Pember et al.*** (***1983***)). The chemoattractant-induced spreading can be seen by the increased cell footprint area post-stimulation (***Figure 1***E). This raises the question of whether the swelling is downstream of spreading and motility. To address this point, we used Latrunculin B to depolymerize the actin cytoskeleton and found that while chemoattractant-induced swelling is unaffected, motility was completely blocked (***Figure 1—figure Supplement 2***A-E; ***Figure 1—video 1***). These data suggest that while chemoattractant simultaneously drives the cell volume increase and the motility changes, these processes are separable from one another.

While the volume of the median cell increases significantly following chemoattractant stimulation, this masks more complex behavior at the single cell level. Single-cell analyses reveal that even as the baseline volume has increased post-activation, individual cells exhibit large fluctuations in volume on the single-minute time scale as they move (***Figure 1***F; ***Video 2***). These fluctuations appear correlated with the neutrophil motility cycle and require an intact actin polymerized cytoskeleton (***Figure 1—figure Supplement 2***F, G). The increase in the volume set point (from 2 mins to 20-30 mins) is closely correlated with the increases in cell velocities over the same time frame (***Figure 1***G). To investigate whether there is a causal link between the chemoattractant-induced cell swelling and migration potentiation, we next sought to identify the molecular regulators of neutrophil swelling.

Video 1. Primary human neutrophils show a biphasic volume response to chemoattractant stimulation
Left panel shows the individual cells (cyan solid lines) with their individual localities (dashed lines). The actual FxM signal is visible within the cell footprints. The video is 40 minutes long with chemoattractant uncaging after the first 10 minutes. The scale bar is 50 um. The right panel shows the corresponding median volume of the population (cyan) with the 95% confidence interval (light cyan). The volume is relative to the average over the two minute window prior to uncaging.
Video 1—source data 1. Data available via DataDryad; see https://doi.org/10.7272/Q6NS0S5N

Video 2. Single cell volume tracking reveals motility-associated volume changes in migrating primary human neutrophils

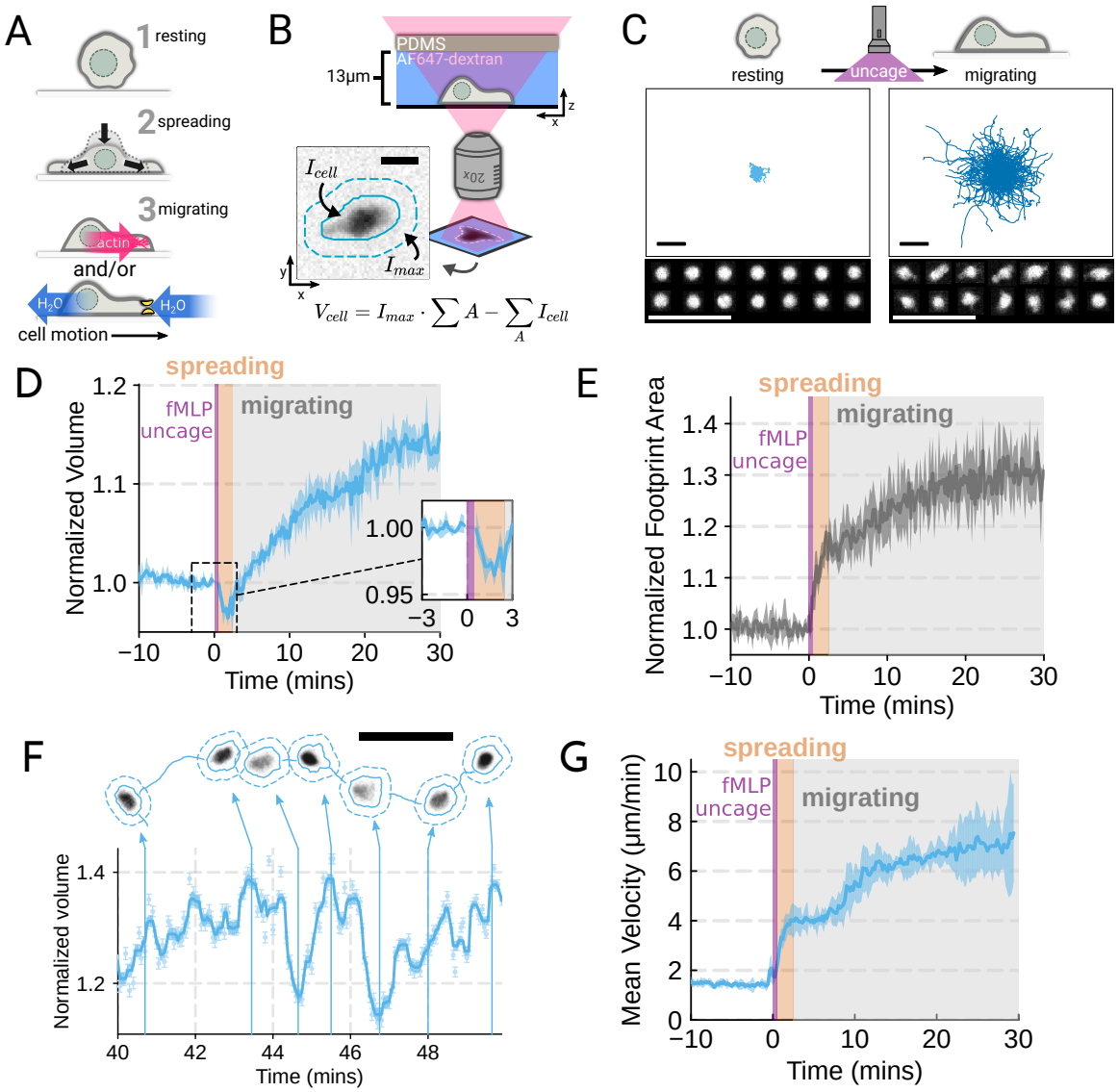

Figure 1. Chemoattractant stimulation elicits competing volume responses in primary human neutrophils
(**A**) Schematic detailing the neutrophil activation process. (**B**) Schematic detailing the Fluorescence Exclusion Microscopy (FxM) approach for measuring single cell volumes, which relies on cells displacing an extracellular dye in a shallow microfluidic chamber. The inset shows an example cell with the cell footprint and local background indicated by the solid or dashed teal lines, respectively. The scale bar is 10um. (**C**) Primary human neutrophil tracks over 15 minute time windows before (left) and after (right) the uncaging of the fMLP chemoattractant. Randomly selected example cells in the bottom panel show neutrophil shape before and after activation. All scale bars are 50um. (**D**) Normalized volumes of primary human neutrophils in response to chemoattractant stimulation (Volunteer N = 4, Cells = 440 total). Inset details the volume loss due to spreading immediately after uncaging. Cells initially lose volume during the spreading phase following the chemoattractant stimulation and then significantly increase in volume. The line plotted is the average of the median cell response for each volunteer, and the shaded region is the 95% CI of the mean. See ***Video 1*** for an animated version. (**E**) The normalized footprint area of primary human neutrophils responding to chemoattractant. The line is the average across biological replicates of median cell footprint area at each timepoint. The footprint area shows a monotonic increase in response to activation with cell spreading prior to initiation of movement. (**F**) Single representative cell trace imaged with high time resolution to highlight the cell motility-related volume fluctuations. Top section depicts the cell track with the FxM images overlaid at key time points that are linked with cyan arrows to the corresponding volumes in the bottom plot. Bottom section is a scatter plot of the raw volume values, with the thick cyan line depicting the rolling median volume. See ***Video 2*** for an animated version. Scale bar is 50um. (**G**) Mean of the per-replicate median cell velocities computed at each time point. The shaded area is the standard deviation at each time point. Cell migration begins to increase in the early spreading phase following chemoattractant stimulation and then continues to increase over the next 20 minutes following stimulation.

Figure 1—video 1. Inhibiting actin polymerization blocks neutrophil chemokinesis

Figure 1—figure supplement 1. Details and validation of the Fluorescence eXclusion Microscopy pipeline

Figure 1—figure supplement 2. Chemoattractant-induced swelling, but not motility, is independent of actin polymerization.

Top panel shows a representative cell migrating starting at 40 minutes following chemoattractant stimulation. The solid cyan line is the cell track. The cell's footprint is denoted with a solid cyan line while its local background is encapsulated by the dashed cyan line. The scale bar is 50 um. The bottom panel shows the concurrent volume changes with the raw FxM measurements displayed in light cyan and the rolling median is shown in cyan. The volume is normalized to the median cell volume in the two minute window prior to stimulation.

Video 2—source data 1. Data available via DataDryad; see https://doi.org/10.7272/Q6NS0S5N

Genome-wide screen identifies regulators of chemoattractant-induced cell swelling

As an unbiased approach for identifying the regulators of chemoattractant-induced cell swelling, we turned to pooled genome-wide CRISPR/Cas9 screening (***Shalem et al.*** (***2014***)). Our approach relies on creating a population of cells with single gene knockouts and then enriching for the cells that fail to swell following stimulation. The quality of this enrichment is the most critical step for success of these screens (***Nagy and Kampmann*** (***2017***)). A key challenge in adapting pooled CRISPR screening to this context was the lack of highly scalable approaches for accurately separating the cells based on their volumes directly. Although volume is difficult to use as a separation approach, cells can be easily separated by buoyant density (mass over volume), which is related to volume over short timescales. Because neutrophil swelling in suspension results from the uptake of water (***Grinstein et al.*** (***1986***)), stimulated neutrophils exhibit a corresponding decrease in buoyant density (***Pember et al.*** (***1983***)). Buoyant density has been successfully used in other genetic screens, including the identification of secretion-defective mutants in yeast (***Novick et al.*** (***1980***)). Finally, buoyant density is a particularly homogenous parameter at the population-level, with 100-fold less variation than either mass or volume across multiple different cell types (***Grover et al.*** (***2011***)).

To verify the chemoattractant-induced shifts in neutrophil buoyant density in our own hands, we deposited linear Percoll gradients (***Figure 2—figure Supplement 1***A-B) in centrifuge tubes and carefully layered nutridoma-differentiated HL-60s (dHL-60s) onto the gradients in the absence or presence of the chemoattractant fMLP (***Figure 2***A). Stimulating dHL-60s with fMLP and using an optimized centrifugation protocol (***Figure 2—figure Supplement 1***C) led to a robust, long-term decrease in buoyant density across millions of cells with a shift in population position clearly visible by eye (***Figure 2***B). The buoyant density change corresponded to a 15% increase in cell volume (***Figure 2***C). This effect depends on chemoattractant-based cell stimulation, as knockout of the fMLP receptor FPR1 completely inhibits fMLP-induced swelling (***Figure 2***C, right).

To screen for the chemoattractant-induced regulators of cell volume, we transduced HL-60 cells with a commercial genome-wide CRISPR knockout library, differentiated them, and spun the cell population into Percoll density gradients with or without fMLP stimulation. We then fractionated the tubes and partitioned the samples into 3 different groups: low, medium, and high buoyant density (***Figure 2—figure Supplement 1***D). We used next-generation sequencing to determine which CRISPR guides were over-represented in the high-density bin, i.e. which guides prevented swelling, leading to the cells remaining dense following stimulation with fMLP (***Figure 2***D). To verify CRISPR knockout efficacy, we confirmed the systematic depletion of essential genes from the population (***Figure 2—figure Supplement 1***E). Computing median log2-fold enrichment of the guides targeting each gene in the dense bin and plotting this value against the false discovery rate revealed the regulators of chemoattractant-induced cell swelling (***Figure 2***E). The top right corner is occupied by genes that are over-represented in the dense, i.e. non-swelling, bin. The top hit was FPR1, the high affinity GPCR that specifically binds to fMLP to initiate the chemoattractant signaling cascade, confirming the effectiveness of the screen.

Our screen revealed a potential transduction cascade from the chemoattractant receptor to the final effectors of cell swelling, including the sodium-proton antiporter NHE1 (SLC9A1), the chloride-bicarbonate exchanger 2 (AE2, i.e. SLC4A2), the gamma subunit of phosphoinositide 3-kinase (PI3Kγ), and carbonic anhydrase II (CA2) (***Figure 2***F). These hits suggest that the cell swelling cascade begins with fMLP binding to the chemoattractant receptor FPR1, which activates PI3Kγ, which in turn activates NHE1 and AE2, the canonical regulatory volume increase complex (***Hoff-***

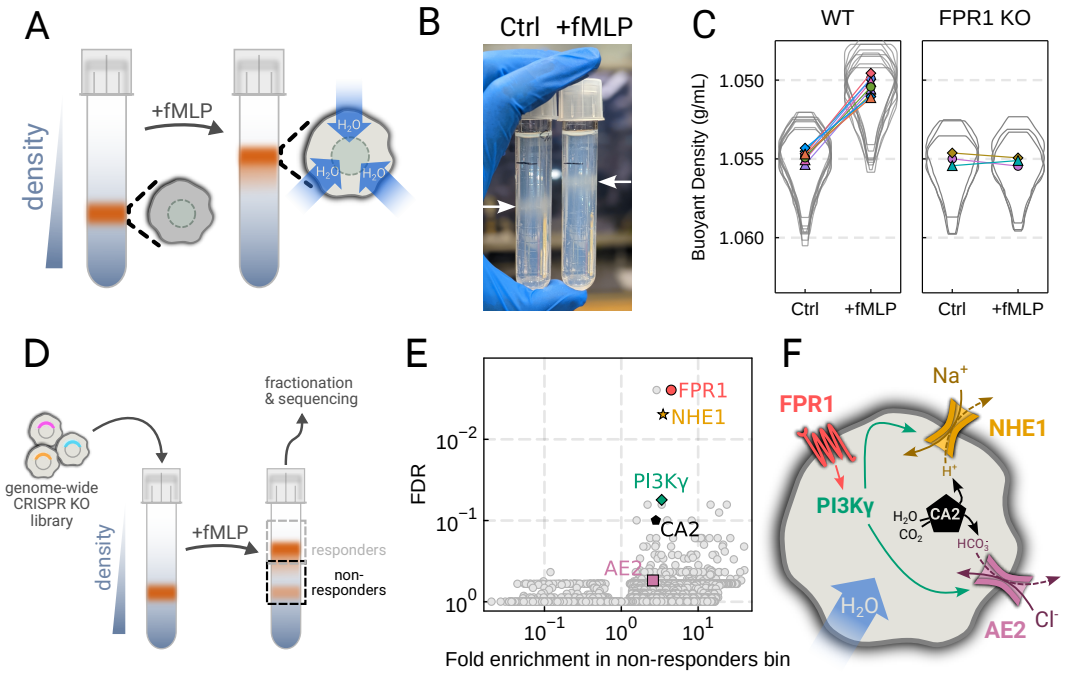

Figure 2. Genome-wide screen identifies regulators of chemoattractant-induced cell swelling
(**A**) Schematic detailing the buoyant density assay. The addition of fMLP causes cells to swell and decrease their density. As a result, the stimulated cells float higher in the Percoll density gradient. (**B**) Representative image of cell density shift following chemoattractant stimulation. Millions of cells appear as white fuzzy bands (indicated with the arrows). Cells in the right tube are stimulated with 20 nM chemoattractant (fMLP), causing them to swell and float higher in the gradient. (**C**) Violin plots quantifying the relative cell numbers as a function of density. Individual lines link replicate pairs. WT cells shift from 1.055g/mL to 1.050g/mL upon stimulation, while FPR1 KO cells do not shift following fMLP stimulation. (**D**) Schematic detailing the buoyant density-based genome-wide CRISPR knockout screen for identifying cells that are deficient at chemoattractant-induced cell swelling. (**E**) Volcano plot of the results of the chemoattractant-induced cell swelling screen. Genes that showed large inhibition of cell swelling and consistent behavior across their targeting guides appear in the upper right. The genes selected for further analysis are highlighted for a more complete list see Table S1. (**F**) Schematic outlining a potential pathway from chemoattractant stimulation to cell swelling.

Figure 2—figure supplement 1. Validation of buoyant density assay and its use in CRISPR KO genome-wide screen for swelling regulators

mann et al. (***2009***)). NHE1 and AE2 would, in this model, eject cytoplasmic protons and bicarbonate ions in exchange for extracellular sodium and chloride, respectively. CA2 catalyzes the production of protons and bicarbonate from CO2 and water and has previously been reported to bind the tail of NHE1, enhancing its activity (***Li et al.*** (***2002***, 2006)). Thus, fMLP binding would lead to a net influx of sodium and chloride into the cell, mediating the influx of water and resulting in cell swelling.

Mechanistically separating chemoattractant versus motility-based volume changes

We next sought to individually validate our hits for chemoattractant-induced swelling. We created and verified single gene knockouts of the four components–NHE1, AE2, PI3Kγ, and CA2–using CRISPR/Cas9 in HL-60 cells. Using our buoyant density assay, we found that loss of either NHE1 or AE2 completely ablated the fMLP-induced volume increase in dHL-60s (***Figure 3***A). Our data indicate that both ion channels are needed for chemoattractant-induced swelling. Knockouts of PI3Kγ and CA2 partially inhibited chemoattractant-induced swelling (***Figure 3—figure Supplement 1***A).

Since dHL-60 cells exhibit significant basal migration even in the absence of chemoattractant stimulation, they are a non-ideal model for investigating chemoattractant-stimulated migration. Primary human neutrophils, on the other hand, are completely quiescent and non-motile prior to

stimulation. We therefore sought to replicate our knockout results through pharmacological inhibition of our screen hits in human primary neutrophils. We used BIX (iNHE1), a potent and selective inhibitor of NHE1 (***Huber et al.*** (***2012***)), and Duvelisib (iPI3Kγ), a dual PI3Kδ/γ inhibitor (***Winkler et al.*** (***2013***)). We compared chemoattractant-stimulated single cell volume responses in unperturbed, NHE1 inhibited (***Figure 3***B), or PI3Kδ/γ inhibited neutrophils (***Figure 3—figure Supplement 1***C). Inhibition of either NHE1 or PI3Kδ/γ prevented chemoattractant-induced swelling in human primary neutrophils. At the single cell level, the NHE1 inhibited population brackets the initial cell volumes even 30 minutes post-stimulation, and this is consistent across days and replicates (***Figure 3***C). To orthogonally verify the volume defect, we used a Coulter counter, an electronic particle sizing method, to measure the single cell volume responses following stimulation in suspension. These experiments confirmed that inhibition of NHE1 blocked cell swelling in suspension as well (***Figure 3—figure Supplement 1***B). NHE1-inhibited cells maintained their ability to change shape and spread in response to chemoattractant, though they lagged behind control cells at later time points (***Figure 3***D). In contrast, PI3Kδ/γ inhibition attenuated both the chemoattractant-induced volume change and the shape change (***Figure 3—figure Supplement 1***B-D).

Blocking NHE1 activity did not interfere with the spreading-induced volume loss of primary human neutrophils but it prevented the subsequent chemoattractant-induced volume gain. We next sought to determine whether the oscillatory volume fluctuations associated with the motility-cycle were affected by NHE1 inhibition. Performing high temporal resolution imaging of single cells at later time points (30-50 minutes) following uncaging revealed that the iNHE1 cells exhibit similar motility-coupled volume changes but at vastly different baselines compared to uninhibited cells (***Figure 3***E; ***Video 3***). Despite the magnitude of the motility-cycle-associated volume fluctuations being similar (***Figure 3—figure Supplement 1***E), the baselines are approximately 20% decreased in NHE1 inhibited versus unperturbed cells following chemoattractant stimulation.

Video 3. NHE1-inhibited primary human neutrophils retain the motility-related volume fluctuations but at much lower baseline volumes
Top panel shows a representative cell migrating starting at 30 minutes following chemoattractant stimulation. The solid gold line is the cell track and the cell's footprint is denoted with a solid gold line while its local background is encapsulated by the dashed gold line. The scale bar is 50 um. The bottom panel shows the concurrent volume changes with the raw FxM measurements displayed in light gold and the rolling median is shown in gold. The volume is normalized to the median cell volume in the two minute window prior to stimulation.
Video 3—source data 1. Data available via DataDryad; see https://doi.org/10.7272/Q6NS0S5N

Video 4. NHE1 inhibition blocks chemoattractant-induced cell swelling and impairs chemokinesis
Left panel shows the individual cells (cyan or gold solid lines) with their individual localities (dashed lines). The top left panel are control cells (cyan) and the bottom left are NHE1 inhibited (gold). The actual FxM signal is visible within the cell footprints. The video is 40 minutes long with chemoattractant uncaging after the first 10 minutes. The scale bars are 50 um. The right panel shows the corresponding median volume of the population in cyan and gold for control and iNHE1, respectively. The corresponding 95% confidence interval is in light cyan or gold. The volume is relative to the average over the two minute window prior to uncaging.
Video 4—source data 1. Data available via DataDryad; see https://doi.org/10.7272/Q6NS0S5N

The chemoattractant-driven volume gain is necessary and sufficient for rapid migration

We next sought to leverage our identified volume regulators to probe the relation between cell swelling and motility. Turning again to the FxM assay, we activated primary human neutrophils by uncaging fMLP and measured the average cell velocity over the population (***Figure 4***A). In the first 10 minutes following uncaging, both WT and NHE1-inhibited cells exhibited a similar potentiation of migration. However, after 10 minutes the unperturbed neutrophils continued increasing in velocity, while the iNHE1 cells plateaued. The WT velocity potentiation is closely correlated with the kinetics of swelling. To visualize the volume-velocity relationship, we plotted the average volume

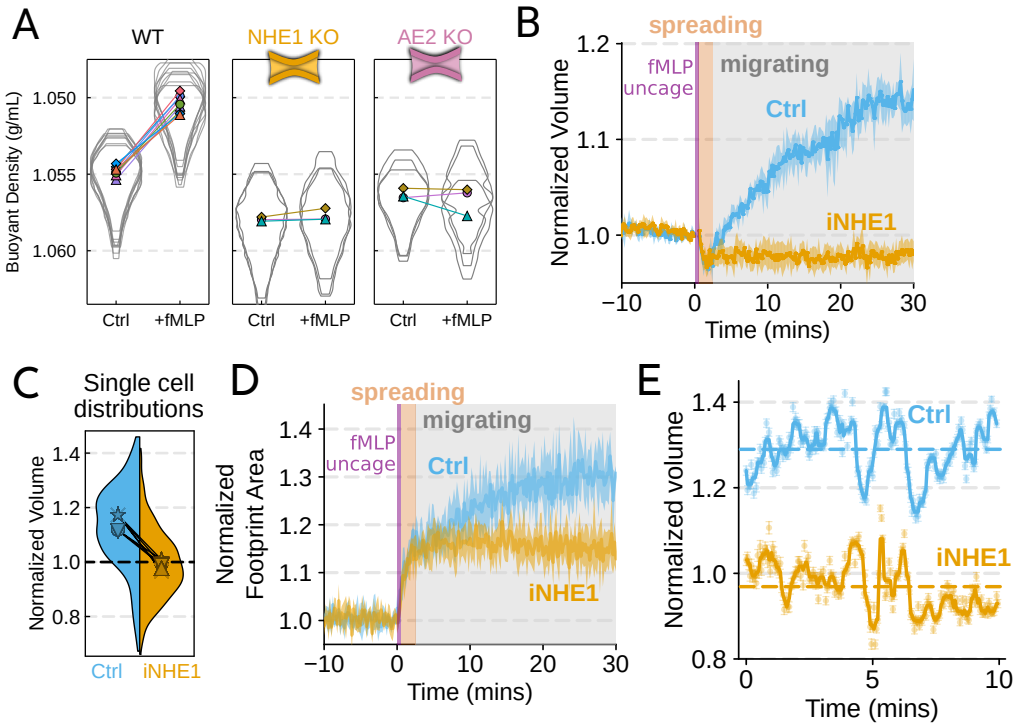

Figure 3. Mechanistically separating chemoattractant versus motility-based volume changes
(**A**) Knockout of NHE1 or AE2 completely inhibits the chemoattractant-induced swelling in neutrophil-like differentiated HL-60 cells. (**B**) NHE1 inhibition in human primary neutrophils blocks fMLP-induced swelling but does not inhibit the spreading-induced volume loss. An animated version is available as ***Video 4***. (Ctrl: Volunteer N = 4, iNHE1: Volunteer N = 6). (**C**) The distributions of single cell volumes 30 minutes post-chemoattractant stimulation demonstrates that the NHE1 inhibited neutrophils remain close to the pre-stimulation volumes, i.e. 1.0 on the ordinate. (**D**) NHE1 inhibited neutrophils have similar increases in their footprint area when they spread and begin moving following fMLP stimulation. (**E**) High temporal resolution imaging of the motility-induced volume fluctuations starting at 30 minutes post-stimulation demonstrate that both control and NHE1-inhibited neutrophils show similar short-term volume fluctuations around significantly different baselines (dashed lines). For an animated version, see ***Video 2*** and ***Video 3***.

Figure 3—figure supplement 1. Additional validation of swelling screen hits.

versus average velocity of single WT cells in the first 10 minutes following uncaging versus 20-30 minutes post-uncaging (***Figure 4***B). In the early time points following chemoattractant stimulation, control cells operate in a low-volume, low-velocity regime. At later time points following stimulation, control cells operate in a higher-volume high-velocity state. The iNHE1 cells persist in the low-volume, low-velocity state even 20-30 minutes post stimulation (***Figure 4***C). To test whether other aspects of chemokinesis are affected in the iNHE1 cells, we also computed the angular persistence of single cells over 10 micron distance windows and found no difference in between WT and iNHE1 cells (***Figure 4—figure Supplement 1***F). This is in contrast to the PI3Kδ/γ-inhibited cells, which failed to increase their velocity following chemoattractant uncaging (***Figure 4—figure Supplement 1***E) and fail to migrate persistently post-chemoattractant stimulation (***Figure 4—figure Supplement 1***F). The single cell traces (***Figure 4—figure Supplement 1***A-D; ***Figure 4—video 1***) show that a large fraction of the PI3Kδ/γ inhibited cells appear to fail to undergo migration following stimulation, offering a potential explanation for the phenotype. In those cells that do start migrating, we observe normal motility-driven volume fluctuations (***Figure 4—figure Supplement 1***G) despite defective swelling.

NHE1-inhibited cells are defective in both chemoattractant-induced swelling and rapid migration. To determine if the lack of cell swelling is the basis of their migration defect, we sought to rescue cell swelling for iNHE1 cells through a mild hypoosmotic shock. Diluting the media 20% (v/v) with water led to a 15% increase in volume of the iNHE1 cells, approximating the magnitude of swelling elicited by fMLP in control cells (***Figure 4***D). Uncaging fMLP initiated chemokinesis for both iNHE1 and hypo-iNHE1 cells, but the hypoosmotically shocked cells continued accelerating for longer and reached greater sustained velocities (***Figure 4***E; ***Video 5***). Intriguingly, the hypoosmotically shocked cells are precocious in their rapid motility. This is expected, since these cells are pre-swollen prior to stimulation, whereas control cells take longer to reach the high-volume high-velocity state following chemoattractant stimulation. Our data suggest that the water influx following chemoattractant stimulation plays an important role in the potentiation of neutrophil migration (***Figure 4***F).

Video 5. NHE1-inhibition leads to impaired motility versus control, which is rescued by mild hypoosmotic shock

Each panel is a representative video of control, NHE1-inhibited, and hypoosmotically shocked NHE1-inhibited cells, respectively. Each video is 40 minutes long and chemoattractant uncaging occurs after 10 minutes. Scale bars are 50 um.

Video 5—source data 1. Data available via DataDryad; see https://doi.org/10.7272/Q6NS0S5N

Discussion

Rapid migration is key to the innate immune function of neutrophils (***Lämmermann et al.*** (***2013***)). Here we show that human primary neutrophils actively increase their cell volumes when stimulated with chemoattractant, and this correlates with their potentiation of movement (***Figure 1***). We find that the chemoattractant-induced swelling occurs independently of cell spreading and motility (***Figure 1—figure Supplement 2***), enabling us to isolate and study the specific role of the swelling on migration. We performed an unbiased genome-wide screen to identify the molecular components of chemoattractant-induced cell swelling (***Figure 2***D-F). While AE2 and particularly, NHE1, have been investigated in previous studies (***Li et al.*** (***2021***); ***Ritter et al.*** (***1998***); ***Denker and Barber*** (***2002***); ***Frantz et al.*** (***2007***); ***Zhang et al.*** (***2022***)), our work systematically identifies the dominant players in a larger network that contribute to the swelling response. Buoyant density screening was used with great success by Schekman and colleagues to elucidate the secretory pathway in yeast (***Novick et al.*** (***1980***); ***Novick and Schekman*** (***1979***)). Here, we use the sensitivity of this assay combined with the power of modern forward genetics to uncover the mechanistic basis of how cells actively manipulate their volume to enhance migration. Similarly to how fungi and plant cells

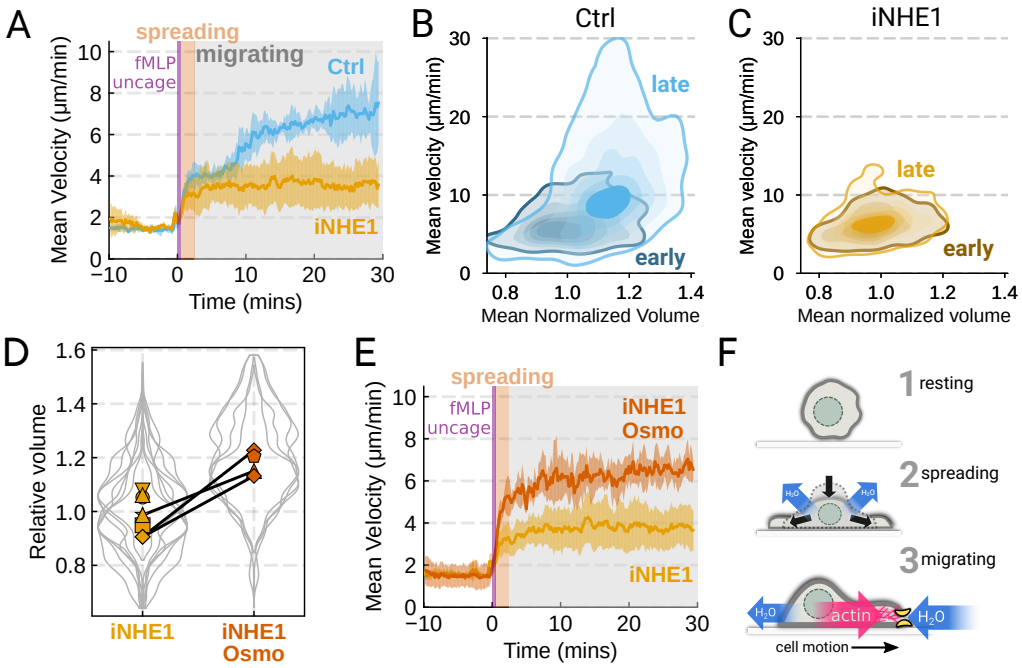

Figure 4. The chemoattractant-driven volume gain is necessary and sufficient for rapid cell migration following stimulation

(**A**) Comparison of control (blue) or NHE1-inhibited (yellow) primary human neutrophil migration following chemoattractant stimulation. Mean of the per-replicate median cell velocities is shown, with the shaded area indicating standard deviation at each time point. (Ctrl: Volunteer N = 4, iNHE1: Volunteer N = 6). (**B**) Contour plots of the average velocity versus average normalized volume for single unperturbed neutrophils for the initial 10 minute window following stimulation (early) and from 20-30 minutes following stimulation (late). (**C**) Contour plots of the average velocity versus average normalized volume for single NHE1-inhibited neutrophils for the initial 10 minute window following stimulation (early) and from 20-30 minutes following stimulation (late). (**D**) Dilution of imaging media with 20% water led to a ~15% increase in the median cell volumes of iNHE1 cells (iNHE1 Osmo; red) versus iNHE1 cells in normal media (yellow). Volumes are normalized relative to the median iNHE1 cell volume. This is similar to the magnitude of chemoattractant-induced swelling in control cells. The black lines connect conditions where both conditions were measured for the same volunteer. (iNHE1 Osmo: Volunteer N = 3, 4 total replicates; iNHE1: Volunteer N = 6) (**E**) Testing the ability of cell swelling to rescue the migration defect in NHE1-inhibited neutrophils. Mean of the pre-replicate median cell velocities computed at each time point for NHE1 inhibited cells (yellow) versus mildly hypoosmotically swollen NHE1 inhibited cells (red). Shaded area is the standard deviation at each time point. (iNHE1 Osmo: Volunteer N = 3, 4 total replicates; iNHE1: Volunteer N = 6). See ***Video 5*** for representative chemokinetic behavior. (**F**) Summary schematic. Cell swelling collaborates with actin polymerization to potentiate chemoattractant-induced cell migration.

Figure 4—video 1. Inhibiting PI3Kγ signaling interferes with neutrophil chemokinesis

Figure 4—figure supplement 1. Additional validation of motility phenotypes.

balance cell wall mechanics with hydraulics to control cell expansion (***Dumais*** (***2021***)), animal cells could use water flows to enhance cytoskeletal dynamics during motility.

Our work implicates both NHE1 and AE2 in cell swelling, as knockout of either completely ablates chemoattractant-induced swelling in dHL-60 cells (***Figure 3***A). Similarly, knockouts of CA2 and PI3Kγ reduced the degree of swelling (***Figure 3—figure Supplement 1***A). We then confirmed our dHL-60 results via pharmacological inhibition in human primary neutrophils. We found that PI3Kδ/γ inhibition interfered with both swelling and chemokinesis in primary human neutrophils (***Figure 3—figure Supplement 1***B-D; ***Figure 4—figure Supplement 1***D-F). Additionally, we verified the necessity of NHE1 in the chemoattractant-induced swelling response (***Figure 3***). NHE1-inhibited cells showed a defect in both motility and chemoattractant-induced swelling (***Figure 4***A-C). At longer time points, NHE1-inhibited cells fail to continue their migration acceleration compared to uninhibited cells. This lack of migration potentiation in NHE1-inhibited cells can be explained by their defective cell swelling, as exogenous swelling via hypoosmotic shock rescues the velocity defect (***Figure 4***E).

How might swelling contribute to rapid cell migration? Given that neutrophils are approximately 65% water (***Figure 2—figure Supplement 1***F), the 15% increase in cell volume corresponds to almost a 25% increase in the water content of the cell after 20 minutes. This change could affect global biophysical parameters by decreasing cytoplasmic viscosity or increasing the diffusion of biochemical or cytoskeletal regulators of movement. Alternatively, local net water influx could collaborate with the actin polymerization machinery in facilitating the extension of the plasma membrane (***Mitchison et al.*** (***2008***); ***García-Arcos et al.*** (***2022***)). The regulatory volume components identified here are ubiquitously expressed, so it is possible that they also facilitate chemoattractant-induced migration in other contexts. NHE1-dependent swelling has been observed in dendritic cells responding to LPS (***Rotte et al.*** (***2010***)), and NHE1 inhibition slows microglial chemotaxis (***Shi et al.*** (***2013***)). NHE1's role in migration and metastasis is well-established (***Stroka et al.*** (***2014***); ***Zhang et al.*** (***2022***); ***Klein et al.*** (***2000***); ***Denker and Barber*** (***2002***)), but whether it plays an active role or merely passively maintains the cytoplasmic pH is still debated (***Hayashi et al.*** (***2008***)). Our experiments indicate that NHE1's active role in the cell swelling program is critical to the potentiation of migration. The other constituents of our chemoattractant-induced cell swelling program have also been implicated in cell migration. AE2 plays a role in murine osteoclast spreading and migration (***Coury et al.*** (***2013***)). Similarly, carbonic anhydrases have been implicated in enhancing NHE1 activity (***Li et al.*** (***2006***)) and facilitating migration (***Svastova et al.*** (***2012***)), and PI3K isoforms have a well-appreciated role in migration (***Ferguson et al.*** (***2007***); ***Devreotes and Horwitz*** (***2015***)). Systematic investigation of this chemoattractant-induced cell swelling network could reveal a general role for water influx in potentiating animal cell migration.

Acknowledgements

We thank Andrea Eastes, Ram Adar, and Kate Cavanaugh for a critical reading of the manuscript, and all members of the Weiner lab for their support and discussions. We also thank Larisa Venkova and Matthieu Piel for the custom shallow FxM mold used in this work. This work was supported by a NSF Graduate Research Fellowship (TLN), UCSF Discovery Fellowship (TLN), an American Heart Association Predoctoral Fellowship (ES), National Institutes of Health grant GM118167 (ODW), National Science Foundation/Biotechnology and Biological Sciences Research Council grant 2019598 (ODW), the National Science Foundation Center for Cellular Construction (DBI- 1548297, ODW), and a Novo Nordisk Foundation grant for the Center for Geometrically Engineered Cellular Systems (NNF17OC0028176, ODW). Sequencing was performed at the UCSF CAT, supported by UCSF PBBR, RRP IMIA, and NIH 1S10OD028511-01 grants.

Author contributions

TLN and ODW conceived the study. TLN and ES conducted the experiments. TLN performed the data analysis. TLN and ODW interpreted the results and wrote the manuscript. All authors edited and approved the final manuscript.

Methods and Materials

Medias and Inhibitors

For all imaging experiments, imaging media was made with Phenol Red-free Leibovitz's L-15 media (Gibco #21083027) supplemented with 10% (v/v) heat-inactivated fetal bovine serum (Gibco) and filtered with a 0.22 um Steriflip filter (MilliporeSigma #SCGP00525). Imaging media was always prepared fresh on the same day of imaging. For washing FxM chips, 0.2% endotoxin and fatty acid-free Bovine Serum Albumin (BSA) (Sigma #A8806) was dissolved in L15 via pulse centrifugation. The mix was then filtered with a Steriflip filter before further use. For all density experiments, divalent-free mHBSS media was prepared as in ***Houk et al.*** (***2012***). In short, 150 mM NaCl, 4 mM KCl, 10 mg/mL glucose and 20 mM HEPES were dissolved in Milli-Q (Millipore) water and the pH adjusted to 7.2 with 1M NaOH. The osmolarity was verified to be 315 mOsm/kg on a micro-osmometer (Fiske Model 210). Culturing media (R10) was made from RPMI 1640 media (Gibco #11875093) supplemented with 25mM HEPES and L-glutamine supplemented with 10% (v/v) heat inactivated fetal bovine serum (Gibco). The NHE1 inhibitor, BIX (Tocris #5512), was dissolved in dry DMSO to a final concentration of 25 mM and stored at -20°C in single use aliquots that were diluted in imaging media the day of the experiment. All iNHE1 experiments used BIX at a 5 uM final concentration. Similarly, Latrunculin-B (Sigma #428020) was stored at 10 mM in DMSO and used at 1 uM final. For PI3Kδ/γ inhibition, Duvelisib (MedChemExpress #HY-17044) was stored at 10 mM in DMSO and used at a final concentration of 1 uM.

Human primary neutrophil isolation and drug treatment

All blood specimens from patients were obtained with informed consent according to the institutional review board-approved study protocol at the University of California - San Francisco (Study #21-35147), see Table S2 for demographic information. Fresh samples of peripheral blood from healthy adult volunteers were collected via a 23-gauge butterfly needle collection set (BD #23-021-022) into 10 ml Vacutainer EDTA tubes (BD #366643). Blood was kept on a shaker at minimum setting and utilized within 2 hours of the draw. Neutrophils were isolated using the EasySep Direct Human Neutrophil Isolation Kit (STEMCELL Tech #19666) with the BigEasy magnet (STEMCELL Tech #18001) according to the manufacturer's protocol.

Isolated neutrophils were spun down at 200xg for 5 min and resuspended in a dye media consisting of imaging media containing 5ug/ml Hoechst 3334 (Invitrogen #H3570) and 0.25 uM Calcein Red-Orange AM (Invitrogen #C34851). This cell suspension was incubated at room temperature in the dark for 15 min, and then the cells were spun down at 200g for 5 min. The dye medium was aspirated and replaced with R10 to achieve a final cell density at or below $1x10^6$ cells/mL. Purified neutrophils were then kept in polystyrene T25 flasks (Corning) at 37°C in a 5% CO2 environment until imaging. Cells were used ~5-8 hours post-isolation.

Cell culture

Short tandem repeat authenticated HL-60 cells (***Saha et al.*** (***2023***)) were maintained in R10 media at 5% CO2 and 37°C and at a concentration of 0.2-1 million/mL by passaging them every 2-3 days. 5 days prior to experiments, HL-60s were differentiated into a neutrophil-like state by taking an aliquot of cells in their culturing medium and supplementing with an equal volume of Nutridoma-CS (Roche #11363743001) and DMSO diluted in RPMI such that that the final concentrations were 0.2 million/mL HL-60 cells, 2% (v/v) Nutridoma-CS, 1.3% (v/v) DMSO, 5% (v/v) FBS in RPMI. After 5

days at 37°C/5% CO2, we observed robust expression of terminal differentiation markers like FPR1 as reported previously (***Rincón et al.*** (***2018***)).

Lenti-X HEK-293Ts (Takara) were used for lentivirus production and maintained at below 80% confluency in DMEM supplemented with 10% (v/v) heat-inactivated fetal bovine serum. These cells were also maintained at 5% CO2 and 37°C. All cell lines were routinely monitored for mycoplasma contamination using standard mycoplasma monitoring kits (Lonza).

FxM single cell volume measurements

FxM microfluidic chips were prepared as previously described (***Zlotek-Zlotkiewicz et al.*** (***2015***); ***Cadart et al.*** (***2017***)) using a custom mold generously provided by the Piel lab. Briefly, 10:1 (w/w) PDMS elastomer base and crosslinker (Momentive #RTV615-1P) were thoroughly mixed, poured into the FxM mold, and degassed under a vacuum for one hour. The PDMS was then baked at 80°C for 2 hours and removed from the mold. The day prior to experiments, the molded PDMS was cut with a scalpel to form 3 lane "chips" and the inlet and outlet holes were created using a 0.5mm punch. The chips and 35mm glass-bottomed dishes (Willco Wells #HBST-3522) were then plasma cleaned for 30 s, and chips were gently pressed down onto the glass to form a watertight seal. A good seal was verified visually by the refractive index change upon glass/PDMS contact. The chips were then baked at 80°C for 10 minutes to ensure thorough bonding. The chips were then quickly coated with 100 ug/mL human fibronectin (Sigma #SLCL0793) diluted in PBS and injected using a pipette tip. Coating was allowed to proceed for 30 minutes at RT before the chamber was flushed with imaging media. The chips were then submerged in PBS and allowed to incubate with L15 + 0.2% BSA overnight at 4°C.

On the day of the experiment, pre-prepared microfluidic chips were allowed to warm up at RT. Human primary neutrophils were gently pipetted up and down to resuspend if they had settled and spun down at 200xg for 4 minutes. The cell pellet was very slowly resuspended in imaging media to achieve a cellular concentration of 60 million per mL. The cells were allowed to equilibrate for 30 minutes at RT. This step helped reduce gas production by the cells that caused problematic laminar flows in our chips. The lanes of the chip were flushed with the corresponding final media. The cells were gently mixed with a 2x solution such that the final concentrations were 0.5mg/mL Alexa Fluor 647-tagged 10,000 MW dextran (Invitrogen #D22914), 200nM caged fMLP (NEP), and 30 million per mL cells in imaging media. This mixture was then slowly pulled into the chamber using a partially depressed pipette tip to minimize the shear forces on the cells, as these are known to affect neutrophil response to fMLP (***Mitchell and King*** (***2012***)). Once loading was complete, the entire chamber was submerged in imaging media to stop all flows and allowed to warm up to 37°C . Experiments were started promptly 20 minutes post-submersion.

Suspension cell volume measurements

Suspension cell volume measurements were performed as in ***Graziano et al.*** (***2019***). Briefly, human primary neutrophils were spun out of culture media at 200xg for 4 minutes and gently resuspended in mHBSS. They were then diluted to 20,000 cells/mL in warm 15mL of mHBSS in Accuvettes (Beckman-Coulter). The cells were incubated at 37°C for 5 minutes, and then either a DMSO blank or the indicated amount of drug was added to the correct final concentration. The cells were again incubated for 5 minutes at 37°C. They were then quickly transported to the Multisizer Z2 instrument (Beckman-Coulter) at RT. Three time points were taken to set a baseline, and then fMLP (Sigma) was added to a final concentration of 20 nM, and the Accuvette was inverted to mix. Then 0.5 mL samples were taken continuously every minute using a 100 um diameter aperture with a current of 0.707 mA, a gain of 64, a pre-amp gain of 179.20, a calibration factor (Kd) of 59.41 and a resolution of 256 bits. 5000-10,000 cells were sampled per time point and the medians of the population was extracted using our software available at https://github.com/tlnagy/Coulter.jl

Buoyant Density Measurements

Buoyant density measurements were done by pre-pouring gradients, layering dHL-60s on top, centrifuging, fractionating, and then imaging to count cells. First, solutions were made with either 32.6% or 57% (v/v) Percoll (Sigma) with 10% (v/v) 10x divalent-free mHBSS and diluted with ultrapure water, making a low density solution (LDS) and high density solution (HDS), respectively. The refractive index of both solutions was determined with a MA871 refractometer (Milwaukee Instruments) as 1.3419 and 1.3467, respectively. Given that the density is linearly related to the refractive index (***Figure 2—figure Supplement 1***A) the solutions have densities of 1.045 g/mL and 1.074 g/mL, respectively. For the chemoattractant-condition, 20 nM fMLP (Sigma) was added. A linear gradient mixer was attached to an Auto Densi-Flow (Labconco) gradient fractionator and used to dispense gradients into 14 mL round bottom tubes (Falcon #352041).

For each gradient, approximately 5 million dHL-60s were spun down at 200xg for 4 minutes and resuspended in 1mL of 1x mHBSS. The cells were then labeled with 0.5 μM Calcein-AM (Invitrogen) for 5 minutes then spun down and resuspended in LDS. For mixed populations, the two cell types were spun down and labeled separately with either Calcein-AM or Calcein Red-Orange-AM and then mixed together. The cells were layered gently on top of the gradient and spun at 250xg for 1 hour. Neutrophils display homotypic aggregation when activated during centrifugation (***Simon et al.*** (***1990***)) so we used a divalent-free media and very long centrifugation times optimized for separation at low centrifugation speeds (***Figure 2—figure Supplement 1***C).

After centrifugation, the cells were fractionated into a 96-well using the Auto Densi-Flow in "remove" modality and a homemade fractionator. 6-7 wells were taken, and their refractive index was measured using the refractometer to align the gradients and verify linearity (***Figure 2—figure Supplement 1***B). A 2x volume of blank media was added to each well to reduce the density, and then the plates were spun in the centrifuge at 250xg to assist the settling of the cells on the glass. The plates were then imaged using confocal microscopy to determine the number of cells in each well. For mixed population experiments, dual color imaging was done to determine the cell count of each population.

CRISPR Genome Wide Screen on Buoyant Density

Lenti-X 293Ts (Takara) were transfected with the Guide-it library (Takara) according to the manufacturer's instructions and concentrated ~100x using the Lenti-X concentrator kit (Takara) and stored at -80°C until needed. Human codon-optimized S. pyogenes Cas9-tagBFP expressing HL-60 cells (***Graziano et al.*** (***2019***)) were transduced by spinoculating the cells on Retronectin-coated (Takara) non-TC treated 6-well plates (Falcon #351146). Briefly, each well was coated with 20ug/mL Retronectin stock solution diluted in DPBS for 2 hours and then blocked with 2% BSA (w/v) in PBS for 30 minutes and washed with PBS. 2mL of 1 million/mL Cas9-BFP HL-60s were added to each well of 4 plates (48 million cells total) and 30uL of concentrated Guide-it library lentivirus was added to each well. Using Lenti GoStix (Takara), we estimated that this corresponds to $8x10^6$ IFUs per well. The plates were spun at 1000xg for 30 mins, and then 1mL of R10 was added gently. This was followed by another dilution with 2 mL of the same media after 24 hours. 48 hours post spinoculation, the cells were spun down at 200xg and resuspended in R10. The cells were then sorted for mCherry-positive cells (cutoff set at 99.9th percentile of the untransduced cell population's mCherry signal) using a FACSAria 3 cell sorter (BD). We observed 4% of cells with a mCherry positive signal, equivalent to a MOI of 0.04. This gives a minimum coverage of 6-24x of the library at transduction; post-sequencing Monte Carlo simulations suggest a minimum coverage of 12x. After sorting, the cells were selected using 175 ug/mL hygromycin and kept in log-phase growth with regular supplementation with fresh media for 7 days, after which ~95% of the population were mCherry positive.

5 days prior to screening day, the cells were differentiated into neutrophil-like cells as described in the "Cell Culture" section. The buoyant density assay was performed as described in the "Buoyant Density Measurements" section with 6 million cells per tube split across 6 tubes, corresponding

to 36 million cells or ~450x coverage of the library. The cells were layered on top of the gradients containing 20 nM fMLP with or without 1 uM Latrunculin-B, and then each tube was fractionated into 48 wells, which were combined into 3 separate bins such that they each contained approximately one third of the population (***Figure 2—figure Supplement 1***D). The bins from each tube belonging to the same sample were combined, and then the cells were spun down, and the pellets were flash frozen to store for further processing.

The genomic DNA was extracted using the QIAamp gDNA kit (Qiagen) according to the manufacturer's instructions. The guides were then PCR amplified for 26 cycles using the Ex Taq polymerase (Takara) protocol with the P5 forward primer mix (Takara) and a unique reverse P7 primer for each condition. The specificity and quality of amplification for each sample was validated using a TapeStation 4200 (Agilent), and the precise DNA concentration was determined using a Qubit fluorometer (Invitrogen) according to manufacturers' instructions. The amplified DNA was then pooled to a 10 nM final concentration followed by a 5% PhiX (Illumina) spike and sequenced in a PE100 run on a HiSeq 4000 sequencer (Illumina) at the UCSF sequencing core.

To verify that we can detect the functioning of Cas9, we assayed for the depletion of guides targeting previously published essential genes (***Wang et al.*** (***2015***); ***Evers et al.*** (***2016***)). We used MAGeCK (***Li et al.*** (***2014***)) to compute the log fold change between the known frequencies of the guides in the library (Takara) and the actual observed frequencies of the guides (computed by pooling all bins together). The cumulative distribution of the essential gene ranks were compared to a randomly shuffling of those same genes to demonstrate that the essential genes were highly depleted from the population, as expected (***Figure 2—figure Supplement 1***E).

Similarly, to determine which genes were involved in the chemoattractant-induced density change, we used MAGeCK to compute the false discovery rate and log fold change between the first and second bins vs the third bin (***Figure 2—figure Supplement 1***D). The third bin was the most dense bin, so genes over-represented in this bin versus the other two were likely interfering with the swelling process. We pooled the samples with and without 1 uM Latrunculin-B together to improve our sensitivity as the swelling is not dependent on a polymerized cytoskeleton (***Figure 1—figure Supplement 2***). The combined fold change for each gene was then computed by taking the MAGeCK "alphamedian" log fold change (either positive or negative) that was most divergent. Using this fold change and the false discovery rate, we identified the genes that are most likely involved with the chemoattractant-induced swelling (***Figure 2***E; Table S1).

Single gene knockout line generation with CRISPR/Cas9

Single gene knockouts were generated and validated using wildtype HL-60s expressing human codon-optimized S. pyogenes Cas9-tagBFP cells as the base line as previously described (***Graziano et al.*** (***2019***)). The two best performing guides from the genome-wide screen (Table S3) were selected and synthesized (IDT) and then cloned into the pLVXS-sgRNA-mCherry-hyg Vector (Takara) following the manufacturer's instructions. Lentivirus was then produced as previously described (***Graziano et al.*** (***2019***)). Briefly, LX-293T cells (Takara) were seeded into 6-well plates and grown till 80% confluence was reached. 1.5 µg of the guide vector (from above) was mixed with 0.167 µg vesicular stomatitis virus-G vector and 1.2 µg cytomegalovirus 8.91 vector. This mixture was incubated with the TransIT-293 Transfection Reagent (Mirus Bio) and used to transfect the 293T cells following the manufacturer's instructions. The cells were grown for 72 hours post-transfection and the virus was concentrated ~40-fold from the supernatant using the Lenti-X concentrator kit (Takara) per the manufacturer's protocol. Concentrated virus stocks were stored at -80°C until needed. For transduction, virus stocks were thawed and added to 300,000 cells in R10 in the presence of polybrene (8ug/mL) and incubated for 24 hours. Afterwards, the cells were washed twice with R10 to remove any remaining viral particles and sorted for mCherry-positivity on a FACSAria 3 cell sorter (BD). The heterogeneous population was then assayed for successful editing by sequencing the genomic DNA flanking the Cas9 cut site. Clonal populations were then isolated by seeding dual BFP and mCherry-positive cells into a 96-well plate such that only one cell was deposited in each

well using a FACSAria Fusion (BD). The cells were then allowed to grow up and clonality was verified by genomic DNA sequencing of the cut site as previously described (***Graziano et al.*** (***2017***)).

Microscopy Hardware

FxM and buoyant density experiments were performed on an inverted Eclipse TI microscope (Nikon) with a Borealis beam conditioning unit (Andor), and light was collected on an air-cooled iXon 888 Ultra EM-CCD (Andor). A 20x Plan Apochromat NA 0.75 objective (Nikon) was used for FxM, and a 10x Plan Apochromat (Nikon) was used for density experiments. Light sources include a Stradus Versalace 405, 488, 561, 647-nm laser line system (Vortran Laser Technologies) and a Sutter Lambda LS xenon-arc lamp used for FxM. Microscopy hardware was controlled with a TriggerScope 4 (Advanced Research Consulting) via MicroManager (***Edelstein et al.*** (***2014***)).

UV light for uncaging was delivered via a 365nm Lambda FLED (Sutter) launched into a Lambda OBC and delivered via the condenser with all mobile optical elements removed and all apertures wide open. Before every experiment, the wattage was measured using a light meter (Thor Labs). The LED was controlled via a custom MicroManager script.

Data Analysis

FxM images were analyzed using a custom pipeline (***Figure 1—figure Supplement 1***A) implemented in the Julia language (***Bezanson et al.*** (***2017***)) available at https://github.com/tlnagy/FluorescenceExclusion.jl. Briefly, the raw images were denoised with a patch-based algorithm (***Boulanger et al.*** (***2010***)) and then the edges were enhanced using a Scharr kernel. The magnitude of the edge values is log normally distributed, and we empirically determined that calling the edge of the cell at 1 standard deviation above the mean gave low noise and the maximum signal (***Figure 1—figure Supplement 1***C). Flood-filling the areas encapsulated by these edges gave a binary mask of the foreground, i.e. space occupied by the cells.

Independently, instance segmentation was performed using a custom Cellpose model trained using the human-in-the-loop feature (***Pachitariu and Stringer*** (***2022***)) on the raw nuclear and cytoplasmic channels. Trackpy was used to link the Cellpose segmented instances together in time (***Allan et al.*** (***2021***)) and these were then used to nucleate a watershed algorithm on the binary mask of the foreground and separate the foreground into the individual tracked cells. Next, the raw image was flatfield corrected by fitting a multiquadratic function at sinusoidally placed locations (avoiding the locations of cells or pillars) in the raw image which gave the densest sampling at the edges. Given that the chambers have flat ceilings supported by pillars (***Zlotek-Zlotkiewicz et al.*** (***2015***)), the background signal can be used to compute the per-time point flatfield. After subtracting the darkfield image from both the raw FxM signal and the interpolant, the raw signal was divided by the interpolant giving extremely uniform homogeneous signal across the FOV.

Next, the local background was computed for each cell which we defined as the region 2 to 10 pixels away (1.3 to 6.5 microns) from the cell borders while avoiding other cells. The median of this local background was used to compute the counterfactual of what the signal would have been if the cell was not there by multiplying by the pixel area of the cell A (***Figure 1***B, inset). The measured signal over the area of the cell was then subtracted from that value to give the volume excluded by the cell according to equation 2 from (***Cadart et al.*** (***2017***)):

$$V_{cell} = \sum_{x,y \in A} \frac{I_{max} - I_{cell}(x, y)}{\alpha} \tag{1}$$

where I_{max} is the median signal of the locality, i.e. the maximum signal if the cell was not there. A is the cell footprint area and I_{cell} is the signal at each point $x, y \in A$. To convert this to absolute volume measurements we divide by α which is the fluorescence as a function of object height:

$$\alpha = (I_{max} - I_{min})/h_{chamber} \tag{2}$$

Where the minimum signal I_{min} is the signal at the pillars that support the chamber's roof and $h_{chamber}$ is the height of the chamber in microns. As discussed in ***Cadart et al.*** (***2017***), while the per-pixel heights might not be accurate due light scatter, segmenting a slightly larger area than the cell footprint (***Figure 1—figure Supplement 1***C) captures any scattered signal and yields accurate whole cell volumes.

For velocity measurements, cell tracks were analyzed using the following equation to compute the velocity at frame i over a window τ given the x and y coordinates in microns and time t in seconds:

$$v_i = \frac{\sqrt{(x_{i+\tau} - x_{i-\tau})^2 + (y_{i+\tau} - y_{t-\tau})^2}}{t_{i+\tau} - t_{i-\tau}} \tag{3}$$

For all plots in this paper a τ of 3 corresponding to approximately a one minute window was used, but similar results were obtained at other values of τ.

To compute angular alignment, we first computed the cumulative distance traveled by each cell at each time-point i. We then computed the angle $\angle$ between each position B_i and positions occupied by the cell prior A_i and subsequent C_i separated by 10 microns of distance traveled by the cell:

$$\text{angular alignment } \angle_i = \text{atan2}\left(\frac{\|\overrightarrow{B_iA_i} \times \overrightarrow{B_iC_i}\|}{\overrightarrow{B_iA_i} \cdot \overrightarrow{B_iC_i}}\right) \tag{4}$$

The angle $\angle_i$ was then re-scaled to be between -1 (complete reversal) and 1 (completely straight) by dividing by π. The results were robust to choice of either distance or temporal offset of A and C from B (data not shown). Finally, to compute the population angular alignment for each time-point, we used the median of $\angle_i$. As expected, the median angular alignment prior to activation is close to 0 as the cells display Brownian motion, but then increases as cells start migrating persistently (***Figure 4—figure Supplement 1***F).

References

Allan DB, Caswell T, Keim NC, van der Wel CM, Verweij RW, soft-matter/trackpy: Trackpy v0.5.0; 2021.

Bezanson J, Edelman A, Karpinski S, Shah VB. Julia: A Fresh Approach to Numerical Computing. SIAM Rev. 2017 Jan; 59(1):65–98.

Boulanger J, Kervrann C, Bouthemy P, Elbau P, Sibarita JB, Salamero J. Patch-based nonlocal functional for denoising fluorescence microscopy image sequences. IEEE Trans Med Imaging. 2010 Feb; 29(2):442–454.

Boyer JS, Silk WK. Review:Hydraulics of plant growth. Funct Plant Biol. 2004 Aug; 31(8):761–773.

Cadart C, Zlotek-Zlotkiewicz E, Venkova L, Thouvenin O, Racine V, Le Berre M, Monnier S, Piel M. Chapter 6 - Fluorescence eXclusion Measurement of volume in live cells. In: Thomas Lecuit, editor. *Methods in Cell Biology*, vol. 139 Academic Press; 2017.p. 103–120.

Collins SR, Yang HW, Bonger KM, Guignet EG, Wandless TJ, Meyer T. Using light to shape chemical gradients for parallel and automated analysis of chemotaxis. Mol Syst Biol. 2015 Apr; 11(4):804.

Coury F, Zenger S, Stewart AK, Stephens S, Neff L, Tsang K, Shull GE, Alper SL, Baron R, Aliprantis AO. SLC4A2-mediated Cl-/HCO3- exchange activity is essential for calpain-dependent regulation of the actin cytoskeleton in osteoclasts. Proc Natl Acad Sci U S A. 2013 Feb; 110(6):2163–2168.

Denk S, Taylor RP, Wiegner R, Cook EM, Lindorfer MA, Pfeiffer K, Paschke S, Eiseler T, Weiss M, Barth E, Lambris JD, Kalbitz M, Martin T, Barth H, Messerer DAC, Gebhard F, Huber-Lang MS. Complement C5a-Induced Changes in Neutrophil Morphology During Inflammation. Scand J Immunol. 2017 Sep; 86(3):143–155.

Denker SP, Barber DL. Cell migration requires both ion translocation and cytoskeletal anchoring by the Na-H exchanger NHE1. J Cell Biol. 2002 Dec; 159(6):1087–1096.

Devreotes P, Horwitz AR. Signaling networks that regulate cell migration. Cold Spring Harb Perspect Biol. 2015 Aug; 7(8):a005959.

Dumais J. Mechanics and hydraulics of pollen tube growth. New Phytol. 2021 Nov; 232(4):1549–1565.

Edelstein AD, Tsuchida MA, Amodaj N, Pinkard H, Vale RD, Stuurman N. Advanced methods of microscope control using μManager software. J Biol Methods. 2014; 1(2).

Evers B, Jastrzebski K, Heijmans JPM, Grernrum W, Beijersbergen RL, Bernards R. CRISPR knockout screening outperforms shRNA and CRISPRi in identifying essential genes. Nat Biotechnol. 2016 Jun; 34(6):631–633.

Ferguson GJ, Milne L, Kulkarni S, Sasaki T, Walker S, Andrews S, Crabbe T, Finan P, Jones G, Jackson S, Camps M, Rommel C, Wymann M, Hirsch E, Hawkins P, Stephens L. PI(3)Kgamma has an important context-dependent role in neutrophil chemokinesis. Nat Cell Biol. 2007 Jan; 9(1):86–91.

Frantz C, Karydis A, Nalbant P, Hahn KM, Barber DL. Positive feedback between Cdc42 activity and H+ efflux by the Na-H exchanger NHE1 for polarity of migrating cells. J Cell Biol. 2007 Nov; 179(3):403–410.

García-Arcos JM, Ziegler J, Grigolon S, Reymond L, Shajepal G, Cattin CJ, Lomakin A, Müller D, Ruprecht V, Wieser S, Voituriez R, Piel M. Advected percolation in the actomyosin cortex drives amoeboid cell motility; 2022.

Graziano BR, Gong D, Anderson KE, Pipathsouk A, Goldberg AR, Weiner OD. A module for Rac temporal signal integration revealed with optogenetics. J Cell Biol. 2017 Aug; 216(8):2515–2531.

Graziano BR, Town JP, Sitarska E, Nagy TL, Fošnarič M, Penič S, Iglič A, Kralj-Iglič V, Gov NS, Diz-Muñoz A, Weiner OD. Cell confinement reveals a branched-actin independent circuit for neutrophil polarity. PLoS Biol. 2019 Oct; 17(10):e3000457.

Grinstein S, Furuya W, Cragoe EJ Jr. Volume changes in activated human neutrophils: the role of Na+/H+ exchange. J Cell Physiol. 1986 Jul; 128(1):33–40.

Grover WH, Bryan AK, Diez-Silva M, Suresh S, Higgins JM, Manalis SR. Measuring single-cell density. Proc Natl Acad Sci U S A. 2011 Jul; 108(27):10992–10996.

Hayashi H, Aharonovitz O, Alexander RT, Touret N, Furuya W, Orlowski J, Grinstein S. Na+/H+ exchange and pH regulation in the control of neutrophil chemokinesis and chemotaxis. Am J Physiol Cell Physiol. 2008 Feb; 294(2):C526–34.

Hoffmann EK, Lambert IH, Pedersen SF. Physiology of Cell Volume Regulation in Vertebrates. Physiol Rev. 2009 Jan; 89(1):193–277.

Houk AR, Jilkine A, Mejean CO, Boltyanskiy R, Dufresne ER, Angenent SB, Altschuler SJ, Wu LF, Weiner OD. Membrane tension maintains cell polarity by confining signals to the leading edge during neutrophil migration. Cell. 2012 Jan; 148(1-2):175–188.

Huber JD, Bentzien J, Boyer SJ, Burke J, De Lombaert S, Eickmeier C, Guo X, Haist JV, Hickey ER, Kaplita P, Karmazyn M, Kemper R, Kennedy CA, Kirrane T, Madwed JB, Mainolfi E, Nagaraja N, Soleymanzadeh F, Swinamer A, Eldrup AB. Identification of a potent sodium hydrogen exchanger isoform 1 (NHE1) inhibitor with a suitable profile for chronic dosing and demonstrated cardioprotective effects in a preclinical model of myocardial infarction in the rat. J Med Chem. 2012 Aug; 55(16):7114–7140.

Klein M, Seeger P, Schuricht B, Alper SL, Schwab A. Polarization of Na(+)/H(+) and Cl(-)/HCO (3)(-) exchangers in migrating renal epithelial cells. J Gen Physiol. 2000 May; 115(5):599–608.

Lämmermann T, Afonso PV, Angermann BR, Wang JM, Kastenmüller W, Parent CA, Germain RN. Neutrophil swarms require LTB4 and integrins at sites of cell death in vivo. Nature. 2013 Jun; 498(7454):371–375.

Lew RR. How does a hypha grow? The biophysics of pressurized growth in fungi. Nat Rev Microbiol. 2011 Jun; 9(7):509–518.

Li W, Xu H, Xiao T, Cong L, Love MI, Zhang F, Irizarry RA, Liu JS, Brown M, Shirley Liu X. MAGeCK enables robust identification of essential genes from genome-scale CRISPR/Cas9 knockout screens. Genome Biol. 2014 Dec; 15(12):1–12.

Li X, Alvarez B, Casey JR, Reithmeier RAF, Fliegel L. Carbonic anhydrase II binds to and enhances activity of the Na+/H+ exchanger. J Biol Chem. 2002 Sep; 277(39):36085–36091.

Li X, Liu Y, Alvarez BV, Casey JR, Fliegel L. A novel carbonic anhydrase II binding site regulates NHE1 activity. Biochemistry. 2006 Feb; 45(7):2414–2424.

620 **Li Y**, Zhou X, Sun SX. Hydrogen, Bicarbonate, and Their Associated Exchangers in Cell Volume Regulation.
621 Frontiers in cell and developmental biology. 2021 Jun; 9:683686. http://dx.doi.org/10.3389/fcell.2021.683686.

622 **Martin KJS**, Muessel MJ, Pullar CE, Willars GB, Wardlaw AJ. The role of phosphoinositide 3-kinases in neutrophil
623 migration in 3D collagen gels. PLoS One. 2015 Feb; 10(2):e0116250.

624 **Metzemaekers M**, Gouwy M, Proost P. Neutrophil chemoattractant receptors in health and disease: double-
625 edged swords. Cell Mol Immunol. 2020 May; 17(5):433–450.

626 **Mitchell MJ**, King MR. Shear-induced resistance to neutrophil activation via the formyl peptide receptor. Bio-
627 phys J. 2012 Apr; 102(8):1804–1814.

628 **Mitchison TJ**, Charras GT, Mahadevan L. Implications of a poroelastic cytoplasm for the dynamics of animal
629 cell shape. Semin Cell Dev Biol. 2008 Jun; 19(3):215–223.

630 **Nagy T**, Kampmann M. CRISPulator: a discrete simulation tool for pooled genetic screens. BMC Bioinformatics.
631 2017 Jul; 18(1):347.

632 **Novick P**, Field C, Schekman R. Identification of 23 complementation groups required for post-translational
633 events in the yeast secretory pathway. Cell. 1980 Aug; 21(1):205–215.

634 **Novick P**, Schekman R. Secretion and cell-surface growth are blocked in a temperature-sensitive mutant of
635 Saccharomyces cerevisiae. Proc Natl Acad Sci U S A. 1979 Apr; 76(4):1858–1862.

636 **Pachitariu M**, Stringer C. Cellpose 2.0: how to train your own model. Nat Methods. 2022 Dec; 19(12):1634–
637 1641.

638 **Pember SO**, Barnes KC, Brandt SJ, Kinkade JM Jr. Density heterogeneity of neutrophilic polymorphonuclear
639 leukocytes: gradient fractionation and relationship to chemotactic stimulation. Blood. 1983 Jun; 61(6):1105–
640 1115.

641 **Rincón E**, Rocha-Gregg BL, Collins SR. A map of gene expression in neutrophil-like cell lines. BMC Genomics.
642 2018 Aug; 19(1):573.

643 **Ritter M**, Schratzberger P, Rossmann H, Wöll E, Seiler K, Seidler U, Reinisch N, Kähler CM, Zwierzina H, Lang HJ,
644 Lang F, Paulmichl M, Wiedermann CJ. Effect of inhibitors of Na+/H+-exchange and gastric H+/K+ ATPase on
645 cell volume, intracellular pH and migration of human polymorphonuclear leucocytes. Br J Pharmacol. 1998
646 Jun; 124(4):627–638.

647 **Rotte A**, Pasham V, Eichenmüller M, Mahmud H, Xuan NT, Shumilina E, Götz F, Lang F. Effect of bacterial
648 lipopolysaccharide on Na(+)/H(+) exchanger activity in dendritic cells. Cell Physiol Biochem. 2010 Oct; 26(4-
649 5):553–562.

650 **Saha S**, Town JP, Weiner OD. Mechanosensitive mTORC2 independently coordinates leading and trailing edge
651 polarity programs during neutrophil migration. Mol Biol Cell. 2023 May; 34(5):ar35.

652 **Sengupta K**, Aranda-Espinoza H, Smith L, Janmey P, Hammer D. Spreading of neutrophils: from activation to
653 migration. Biophys J. 2006 Dec; 91(12):4638–4648.

654 **Shalem O**, Sanjana NE, Hartenian E, Shi X, Scott DA, Mikkelsen TS, Heckl D, Ebert BL, Root DE, Doench JG, Zhang
655 F. Genome-scale CRISPR-Cas9 knockout screening in human cells. Science. 2014 Jan; 343(6166):84–87.

656 **Shi Y**, Yuan H, Kim D, Chanana V, Baba A, Matsuda T, Cengiz P, Ferrazzano P, Sun D. Stimulation of Na(+)/H(+)
657 exchanger isoform 1 promotes microglial migration. PLoS One. 2013 Aug; 8(8):e74201.

658 **Simon SI**, Chambers JD, Sklar LA. Flow cytometric analysis and modeling of cell-cell adhesive interactions: the
659 neutrophil as a model. J Cell Biol. 1990 Dec; 111(6 Pt 1):2747–2756.

660 **Stroka KM**, Jiang H, Chen SH, Tong Z, Wirtz D, Sun SX, Konstantopoulos K. Water permeation drives tumor cell
661 migration in confined microenvironments. Cell. 2014 Apr; 157(3):611–623.

662 **Svastova E**, Witarski W, Csaderova L, Kosik I, Skvarkova L, Hulikova A, Zatovicova M, Barathova M, Kopacek J,
663 Pastorek J, Pastorekova S. Carbonic Anhydrase IX Interacts with Bicarbonate Transporters in Lamellipodia
664 and Increases Cell Migration via Its Catalytic Domain*,. J Biol Chem. 2012 Jan; 287(5):3392–3402.

665 **Svitkina T**. The Actin Cytoskeleton and Actin-Based Motility. Cold Spring Harb Perspect Biol. 2018 Jan; 10(1).

Venkova L, Vishen AS, Lembo S, Srivastava N, Duchamp B, Ruppel A, Williart A, Vassilopoulos S, Deslys A, Garcia Arcos JM, Diz-Muñoz A, Balland M, Joanny JF, Cuvelier D, Sens P, Piel M. A mechano-osmotic feedback couples cell volume to the rate of cell deformation. Elife. 2022 Apr; 11.

Wang T, Birsoy K, Hughes NW, Krupczak KM, Post Y, Wei JJ, Lander ES, Sabatini DM. Identification and characterization of essential genes in the human genome. Science. 2015 Nov; 350(6264):1096–1101.

Weiner OD, Servant G, Welch MD, Mitchison TJ, Sedat JW, Bourne HR. Spatial control of actin polymerization during neutrophil chemotaxis. Nat Cell Biol. 1999 Jun; 1(2):75–81.

Winkler DG, Faia KL, DiNitto JP, Ali JA, White KF, Brophy EE, Pink MM, Proctor JL, Lussier J, Martin CM, Hoyt JG, Tillotson B, Murphy EL, Lim AR, Thomas BD, Macdougall JR, Ren P, Liu Y, Li LS, Jessen KA, et al. PI3K-δ and PI3K-γ inhibition by IPI-145 abrogates immune responses and suppresses activity in autoimmune and inflammatory disease models. Chem Biol. 2013 Nov; 20(11):1364–1374.

Zhang Y, Li Y, Thompson KN, Stoletov K, Yuan Q, Bera K, Lee SJ, Zhao R, Kiepas A, Wang Y, Mistriotis P, Serra SA, Lewis JD, Valverde MA, Martin SS, Sun SX, Konstantopoulos K. Polarized NHE1 and SWELL1 regulate migration direction, efficiency and metastasis. Nat Commun. 2022 Oct; 13(1):1–17.

Zlotek-Zlotkiewicz E, Monnier S, Cappello G, Berre ML, Piel M. Optical volume and mass measurements show that mammalian cells swell during mitosis. J Cell Biol. 2015 Nov; 211(4):765–774.

Supplementary Information

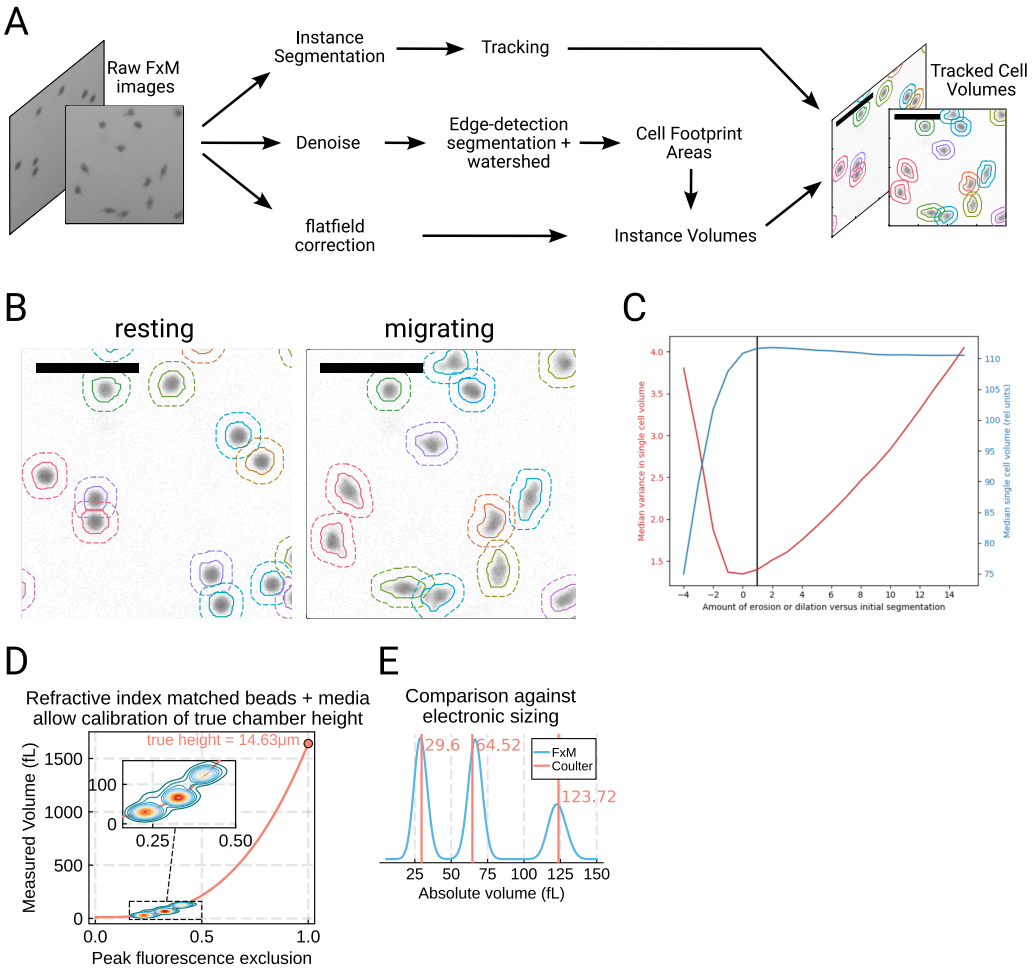

Figure 1—figure supplement 1. Details and validation of the Fluorescence eXclusion Microscopy pipeline

(**A**) Overview of the modified FxM pipeline used in this work. Raw FxM images are segmented into "seeds," which are then tracked. To identify cell boundaries, we use a custom algorithm that involves denoising the raw FxM followed by edge detection and watershedding that was nucleated at the seeds. Finally, to extract the volumes we apply minimal processing with a custom flatfield correction algorithm followed by extraction using the previously-determined cell boundaries. (**B**) Examples of resting (left) and migrating (right) cells segmented and tracked using the aforementioned pipeline. (**C**) Quantifying the signal-to-noise tradeoff with the edge detection. Overly conservative or overly liberal segmentation leads to non-optimal volume measurement. The chosen cutoff (black line) balances the noise (red) and measured volume (blue). This was computed on unstimulated cells. (**D**) Injecting beads into the FxM chambers in refractive-index media to minimize distortions allows for true calibration of chamber height. The contour plot of the per-bead max signal depth (i.e. height of the beads from FxM) vs the measured volume using FxM is well fit by the spherical volume formula (salmon line). The intersection of this line with 1.0 on the abscissa is equivalent to a sphere that completely fills the chambers and indicates the true height of the chamber. (**E**) Comparing calibrated FxM volumes of the beads (cyan) against the gold standard Coulter counter (salmon) shows good agreement.

Ranking	HUGO ID	Fold Change	FDR	# Good sgRNAs	Common Name
1	**FPR1**	**4.4617**	**0.00248**	**3**	**FPR1**
2	STAT3	2.8815	0.00248	4	
3	**SLC9A1**	**3.5013**	**0.00495**	**4**	**NHE1**
4	**PIK3CG**	**3.3557**	**0.05569**	**4**	**PI3Kγ**
5	MARS2	23.6178	0.06374	3	
6	NUP35	14.5253	0.06374	3	
7	SKA1	3.3554	0.06374	4	
8	**CA2**	**2.8157**	**0.09942**	**4**	**CA2**
9	CANX	3.966	0.09942	4	
10	COPS3	8.2426	0.10015	4	
11	RPS2	18.7498	0.07976	3	
12	TPR	9.6024	0.16455	4	
13	RFT1	26.2401	0.16455	2	
14	SETD1A	11.1409	0.16455	2	
15	TP53TG3C	11.2083	0.16455	3	
16	UHRF1	4.7194	0.16455	3	
17	THG1L	10.4411	0.16455	3	
18	MRPL20	10.8506	0.16455	4	
19	UTP11L	9.0882	0.16455	3	
20	TPI1	17.976	0.16455	3	
21	CT47A6	2.8505	0.16455	3	
22	ESCO2	11.9249	0.1982	4	
23	GRXCR2	2.8457	0.1982	4	
24	PARP12	21.181	0.1982	2	
25	NR1H2	39.6651	0.20894	2	
26	PPP2R2A	4.4472	0.20894	4	
27	SLC25A26	20.7941	0.20894	2	
28	GANAB	2.7762	0.20894	3	
29	MMGT1	22.231	0.24088	2	
30	TCEB2	9.1192	0.26382	4	
31	MRPL17	9.465	0.26382	3	
32	C1QB	2.7157	0.26382	4	
33	TMX3	3.0917	0.26382	4	
34	TOPBP1	14.0471	0.16455	3	
35	AP3M1	7.9696	0.26528	2	
36	MSMB	4.5751	0.26528	4	
37	WDR83	5.4812	0.26528	4	
38	MARCH7	6.5514	0.2937	2	
39	RNF111	2.9736	0.2937	4	
40	MOGS	3.5169	0.2937	3	
100	**SLC4A2**	**2.582**	**0.54636**	**2**	**AE2**

Table S1. Chemoattractant-induced swelling genome-wide CRISPR KO screen hits
Rankings determined using MAGeCK *Li et al.* (*2014*). Fold change is the median fold enrichment in the dense bin versus the other two bins of the functional guides. FDR is the false discovery rate of each gene given the distribution of negative control guides in the library. See Methods section for details.

Volunteer	Age	Sex
1	28	F
4	27	M
5	30	M
6	37	F
8	31	M
14	24	M
17	29	F
18	28	M
19	30	M
20	27	M

Table S2. Volunteer Demographic Information
Demographic information collected for the volunteer donors according to the Institutional Review Board-approved study protocol at the University of California - San Francisco (Study #21-35147)

HUGO gene name	Takara sgRNA ID	Guide Sequence (5' -> 3')	Internal ID
FPR1	sgFPR1_2	CTACAGTACCTGGTAAAACG	11
FPR1	sgFPR1_3	CTGACAGCAACGATGGACAT	12
SLC9A1	sgSLC9A1_2	TTTGCCAACTACGAACACGT	13
SLC9A1	sgSLC9A1_4	TGAGGAACAGGTCACACATG	15
PIK3CG	sgPIK3CG_1	ACTTAACCCTCTCACAGCAG	16
PIK3CG	sgPIK3CG_3	GAGAATACGTCCTCCACATG	18
CA2	sgCA2_2	TATGAGTGTCGATGTCAACA	19
CA2	sgCA2_4	TCACTGGAACACCAAATATG	20
SLC4A2	sgSLC4A2_2	ACCTGCCCCACATACCCACA	21
SLC4A2	sgSLC4A2_3	GAAGACGCAGGACCTGATAG	22
NegCtrl	Neg_Control_Human_0067	GGTAGGACCTCACGGCGCGC	23
NegCtrl	Neg_Control_Human_0084	GCTGTCGTGTGGAGGCTATG	24

Table S3. Guides used to make single gene knockouts in HL-60s
The two highest performing guides from the genome-wide screen were chosen to make single gene knockouts in the HL-60 cell line. See Methods for details.

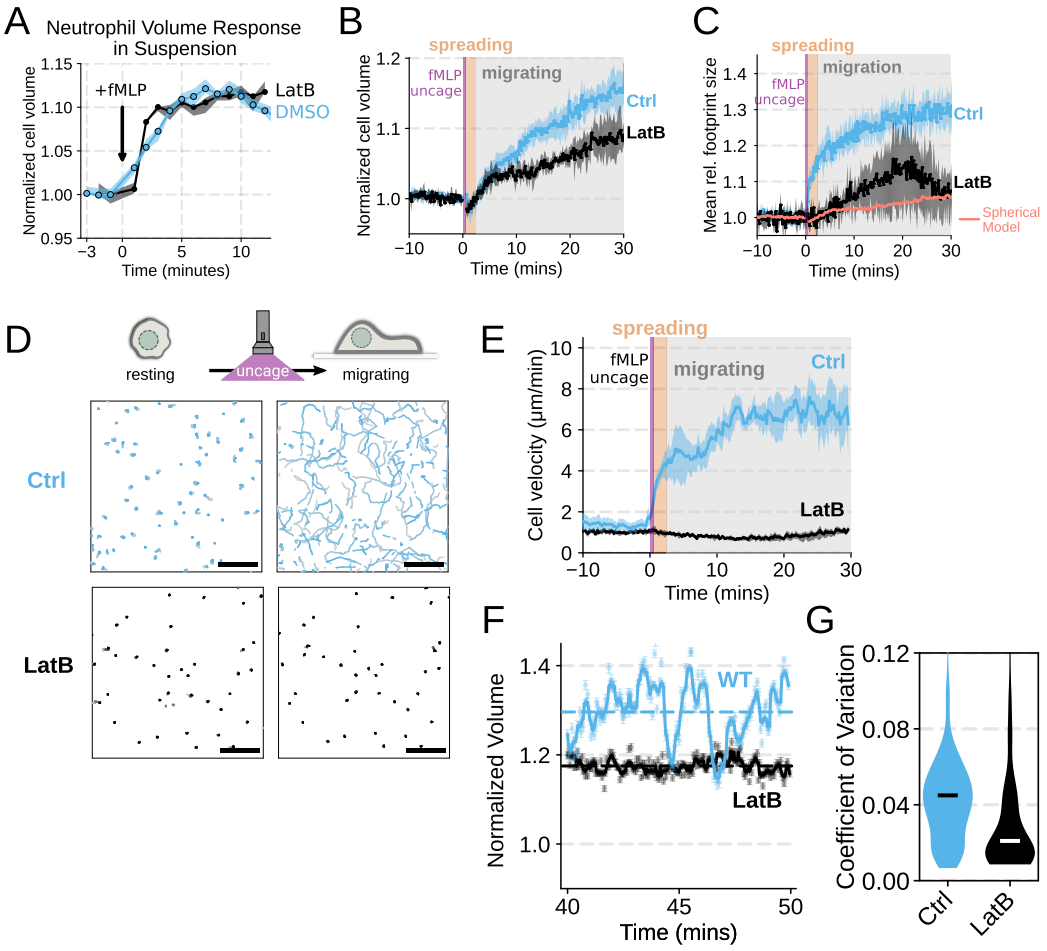

Figure 1—figure supplement 2. Chemoattractant-induced swelling, but not motility, is independent of actin polymerization.

(A) Human primary neutrophils were incubated with DMSO or Latrunculin B, activated with 20 nM fMLP, and then volume responses were measured using electronic sizing via a Coulter counter. Latrunculin treatment did not alter cell swelling, indicating that actin polymerization is dispensable for the chemoattractant-induced volume increase. **(B)** Similar results were obtained using the FxM assay, showing that Latrunculin-treated cells are capable of swelling after stimulation. **(C)** The Latrunculin-treated cells also increase their footprints, albeit less so than control cells, but this is within the range of what would be expected for this degree of chemoattractant-induced volume increase (modeled by a sphere expanding an equivalent volume). **(D)** Single cell tracks of primary human neutrophils responding to acute chemoattractant stimulation. Both panels show 15 minutes of tracks with the tracks prior (left) and the 15 minutes post (right) uncaging the chemoattractant. The scale bar is 50 microns. The top panels show the large increase in motility displayed by control cells, while the Latrunculin-treated cells (bottom panels) fail to move. See ***Figure 1—video 1*** for an animated version of this data. **(E)** Latrunculin-treated cells consistently fail to move in response to chemoattractant-stimulation. **(F)** Representative single cell volume traces show that Latrunculin-treated cells (black) lack short-term volume fluctuations but persistently maintain an elevated volume following chemoattractant stimulation. Control cells (blue) exhibit short-term volume fluctuations. **(G)** The lack of short-term volume fluctuations following latrunculin treatment is borne out across the population, with the coefficient of variation in the volume for single cells (post-swelling) being dramatically lower in Latrunculin-treated cells, suggesting that these short term volume fluctuations depend on actin-based motility.

Figure 1—figure supplement 2—source data 1. Raw and processed Fluorescence Exclusion Microscopy data available via DataDryad; see https://doi.org/10.7272/Q6NS0S5N

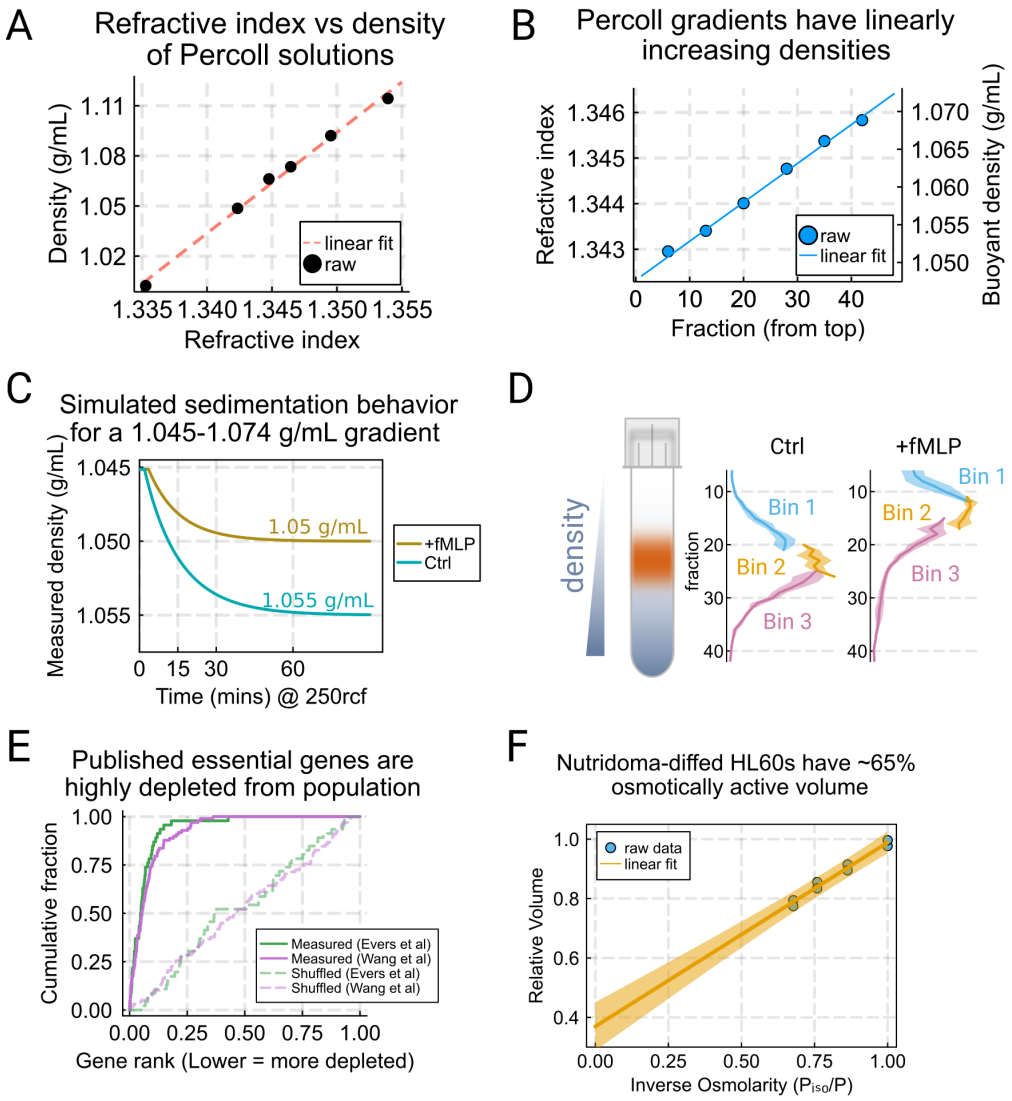

Figure 2—figure supplement 1. Validation of buoyant density assay and its use in CRISPR KO genome-wide screen for swelling regulators

(**A**) Varying the amount of Percoll shows the linear relationship between the refractive index (as measured by a refractometer) and the density as determined by weighing solutions in a volumetric flask on an analytical balance. (**B**) Measuring the refractive index of different fractions from the gradient shows a high degree of linearity in buoyant density. (**C**) Simulation of the settling behavior of the control (teal) and stimulated cells (gold) in the Percoll gradients under a centrifugal force of 250xg. The cells are predicted to arrive at their isopycnic point after approximately one hour. (**D**) The binning strategy for the screen for the control (left) and stimulated (right) conditions. For each replicate of each condition, the cells were split across 6 different tubes and these were combined into 3 bins to balance the minimum number of cells per bin with the resolution gained from multiple bins. (**E**) Previously published essential genes from ***Evers et al.*** (***2016***) and ***Wang et al.*** (***2015***), in green and purple, respectively, were highly depleted from the population, validating functionality of our CRISPR-based knockout library. (**F**) Ponder's relation for dHL-60s in suspension. Increasing amounts of hyperosmolarity drives the osmotically active fraction of the volume out of the cell, and projecting out to infinite osmolarity gives 65% of the cell volume as osmotically active.

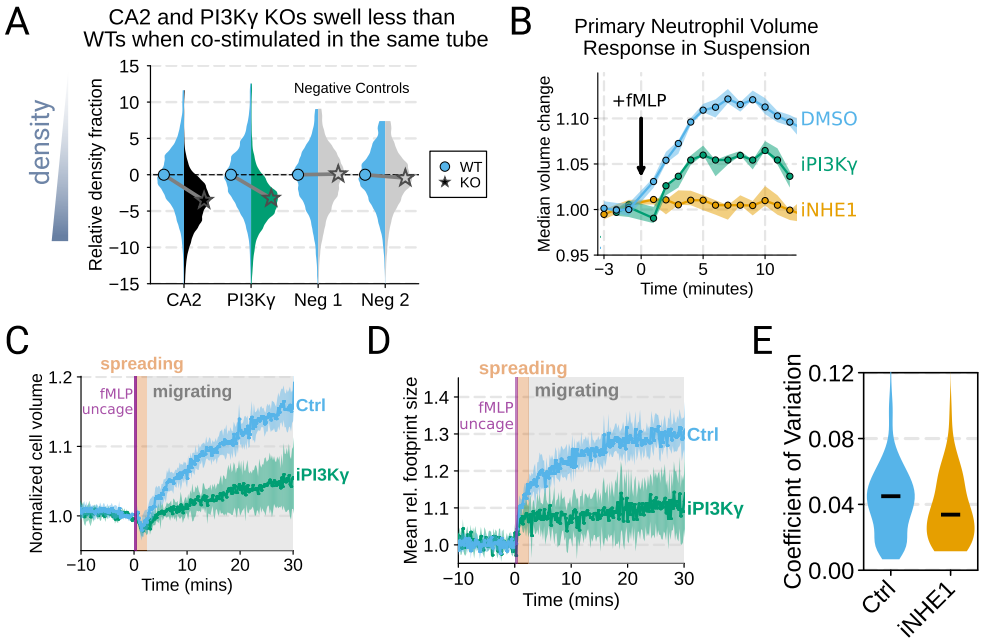

686

Figure 3—figure supplement 1. Additional validation of swelling screen hits.
(A) Mixed WT and CRISPR KO dHL-60 populations post-stimulation show that CA2 (black) and PI3Kγ (green) KO both fail to decrease their densities as much as the WT (cyan) population following chemoattractant stimulation. Cells with negative control guides (light gray) have normal volume responses. All tubes were fractionated and aligned on the fraction containing the median of the WT population. Negative values indicate a fraction with a higher density than WT. **(B)** To validate the perturbations to cell swelling observed with FxM, primary human neutrophils were stimulated in suspension, and their volumes were measured using a Coulter counter. 20 nM fMLP was added at the 0 minute mark. Shaded regions represent the 95% confidence intervals. **(C)** PI3Kγ inhibition blocks the chemoattractant-induced volume change in primary human neutrophils, as assayed by FxM. **(D)** PI3Kγ inhibition also blocked the chemoattractant-drive shape change in human primary neutrophils, as measured by the change in footprint area in FxM. **(E)** The coefficient of variation in volume for control (cyan) and iNHE1 (gold) inhibited human primary neutrophils undergoing chemokinesis are comparable, suggesting that the volume fluctuations are unchanged in moving cells upon NHE1 and PI3Kγ inhibition despite the different baseline volumes.
Figure 3—figure supplement 1—source data 1. Raw and processed FxM and Coulter data available via DataDryad; see https://doi.org/10.7272/Q6NS0S5N

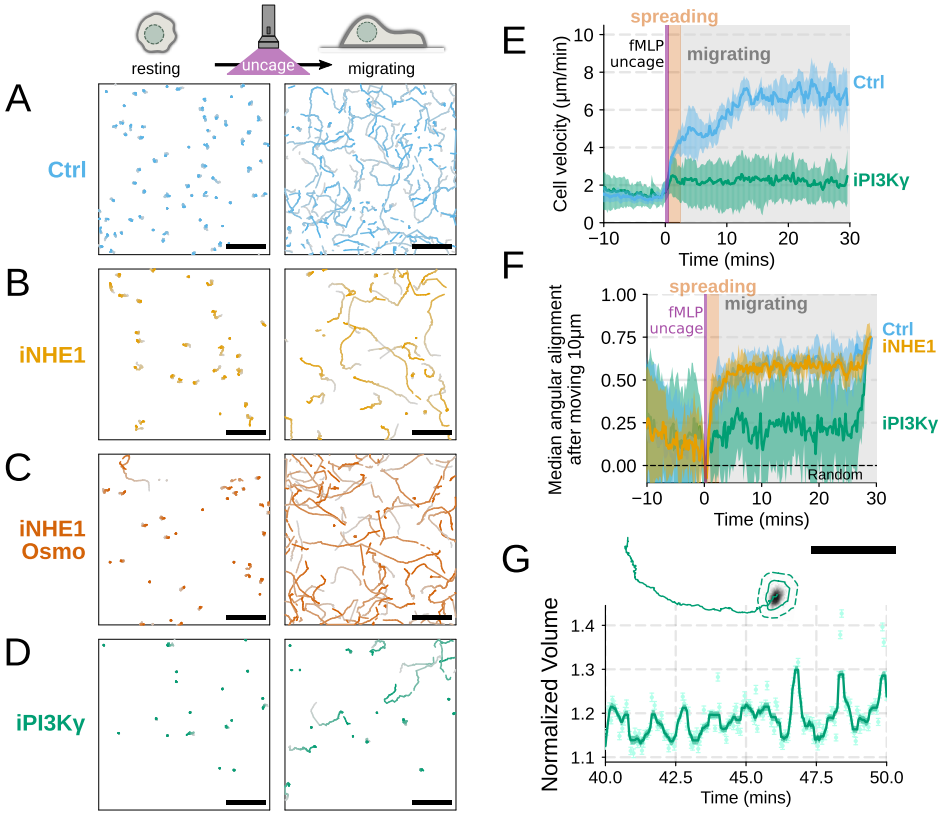

Figure 4—figure supplement 1. Additional validation of motility phenotypes.
(A-D) Single cell tracks of primary human neutrophils responding to acute chemoattractant stimulation. Both panels show tracks of cells 15 minutes prior (left) versus 15 minutes post (right) uncaging the chemoattractant. The scale bar is 50 microns. Color saturation indicates time with tracks progressing from gray to full color. Animated versions are available as ***Video 5*** and ***Figure 4—video 1***. **(A)** Control cells show a large increase in movement upon uncaging, **(B)** NHE1 inhibited cells also initiate movement but to a lesser degree, **(C)** hypo-osmotic shock rescues the NHE1 motility defect. **(D)** PI3Kγ leads to a large fraction of cells failing to initiate movement. **(E)** PI3Kγ inhibition showed near complete blockage of the chemoattractant-induced motility increase in primary human neutrophils. **(F)** Control neutrophils (blue) show an increased angular alignment upon stimulation as their motility becomes directional. NHE1-inhibition (gold, iNHE1) has very little effect on this process, while PI3Kγ inhibition (green) leads to a reduction in this alignment at the population level. **(G)** For the PI3Kγ inhibited cells that start migrating, the migration-induced volume fluctuations are comparable to iNHE1 and control cells. The top panel shows the track of a representative migrating PI3Kγ inhibited cell and the bottom panel, its corresponding volume normalized to the pre-stimulation volume. The scale bar is 50 microns.
Figure 4—figure supplement 1—source data 1. Raw and processed FxM data available via DataDryad; see https://doi.org/10.7272/Q6NS0S5N